Numerical Simulation of Electrostatic Charging Droplets in Microfluidic Devices

Hongbo Zhou[1,2], Shuhuai Yao[*1]

[1] Department of Mechanical Engineering, The Hong Kong University of Science and Technology, Hong Kong, China.
[2] Shanghai Institute of Microsystem and Information Technology, Chinese Academy of Science, 865 Changning Road, Shanghai, China.
*Corresponding Author： Tel: 852 2358 7205; E-mail: meshyao@ust.hk

Abstract
In this paper, the mechanism of charging process was simulated and analyzed. The simulation was conducted using COMSOL Multiphysics®, based on the laminar two-phase flow level-set interface coupling with the electrostatic interface. Meanwhile, different parameters (such as the droplet size and surfactant) were numerical studied. Based on the simulation results, a more efficient charging design was proposed. Finally, microfluidic devices were developed using standard microfabrication technology, and the induced charge in a droplet was characterized in the devices. The experimental results agreed well with the simulation.

Keywords: Level-set method, Droplet, Microfluidics, COMSOL

1 Introduction

Droplets in microfluidic systems can work as 'miniaturized laboratories'[1, 2] for their unique features such as high-throughput, minimal reagent consumption, contamination-free, fast response, and isolation of individual space[3, 4]. Precharged droplets can facilitate manipulation and control of low-volume liquids in droplet-based microfluidics. However, the working principle and charge quantification of the non-contact charging system remains elusive for precise control of droplets in practical systems[5].

In this paper, to realize this non-contact charging method, we performed both numerical and experimental studies for charging droplets in a T-junction microchannel with embedded electrodes. Using numerical methods for two-phase flow coupling with electrostatics, for the first time, the mechanism of charging process was simulated and analyzed.

2 Methods and materials

2.1 Working mechanism

The principle of the droplet charging process in a T-junction microchannel is illustrated in Fig.1. A neutral water droplet travels along the vertical channel and is entering the T-junction bifurcation where a pair of charging electrodes are embedded symmetrically and covered by a dielectric layer. When a positive or negative pulse is applied to the charging electrodes, opposite charges is induced on the water-oil interface (Fig. 1a). Then the droplet is stretched by hydrodynamic force[6] at the T-junction, a cylindrical liquid thread is formed and connects two rears of the droplet at both sides (Fig. 1b). As the stretching process continues, the circumference of the thread becomes thinner gradually, which triggers the onset of the Rayleigh-Plateau instability[6, 7]. In consequence, the liquid thread breaks up, and the induced charges remain in the two separated new droplets (Fig. 1c). In this way, two daughter droplets with opposite net charges are obtained. The total capacitance of the induction electrodes, dielectric layer and the droplet constitute capacitors in series can be estimated as (shown in Fig. 1a), $C_{whole}=C_{interface} \parallel C_{drop} \parallel C_{interface}$, where $C_{interface}$ represents the capacitor formed by the electrode-dielectric layer-droplet interface. And the total capacitance varies as droplet reshapes in the stretching and splitting process. If $V_{charging}$ is applied across the induction electrodes, the induced charge would be $Q = C_{whole}*V_{charging}$ in the A' part and B' part of the droplet. The ultimate charge in droplet A' and B' (Fig. 1c) is determined by the capacitance of the whole system at the instant of droplet separation ($C_{separation}$), $Q = V_{charging}*C_{separation}$. Therefore, it is essential to perform numerical simulation to calculate $C_{separation}$ in the microfluidic devices.

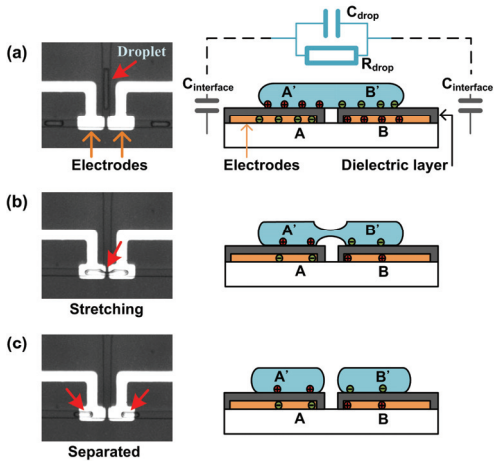

Fig.1 Principle of the charging process. The left column is the top view and the right column is the side view. (a) a neutral droplet travels to the induction electrodes and, charges are induced and distributed on the surface. (b) a droplet is stretched at the T-junction by hydrodynamic force. (c) a droplet is divided into two daughter droplets with opposite net charges.

2.2 Numerical simulation

In order to quantify the amount of induced charge in droplets, we performed numerical simulations to capture the droplet dynamics and variation of the system capacitance during the droplet splitting and reshaping. The simulation was conducted using a commercial finite element code, COMSOL Multiphysics, based on the laminar two-phase flow level-set interface coupling with the electrostatic interface. Forces other than electrostatic forces (e.g., dielectrophoretic, electrowetting electrophoresis, etc) were neglected in our simulation for relatively low electric field (~10^5 V/m).

First, the interface between the immiscible water and oil phases is tracked using the level set method[8], in which the interface is represented by the level set function ϕ [9]. The velocity field of two-phase flow in the simulation is governed by the incompressible Navier-Stokes equations:

$$\frac{\partial \rho}{\partial t} + \nabla \cdot (\rho \vec{u}) = 0 \qquad (1)$$

$$\rho \frac{\partial \vec{u}}{\partial t} + \rho(\vec{u} \cdot \nabla)\vec{u} = -\nabla p + \nabla \cdot (\mu \nabla \vec{u}) + \vec{F}_{st} \qquad (2)$$

$$\rho = \rho_1 + (\rho_2 - \rho_1)\phi\,,\ \mu = \mu_1 + (\mu_2 - \mu_1)\phi \qquad (3)$$

where ρ_1 and ρ_2 are the fluid densities of dispersed phase and continuous phase, u is the flow velocity, t represents the time, p is the pressure, μ_1 and μ_2 denote the dynamic viscosities of dispersed phase and continuous phase. The body force $\vec{F}_{st}$ is caused by the surface tension, $\vec{F}_{st} = \sigma\kappa\delta\vec{n}$, where σ is the interfacial tension between two phases, κ is the curvature, δ is a Dirac delta function concentrated to the interface, and $\vec{n}$ is the unit normal to the interface. The motion of the water-oil interface is tracked by solving the equation for ϕ:

$$\frac{\partial \phi}{\partial t} + u \cdot \nabla \phi = \gamma \nabla \cdot (\varepsilon \nabla \phi - \phi(1-\phi)\frac{\nabla \phi}{|\nabla \phi|}) \qquad (4)$$

where γ determines the amount of reinitialization of the level set function and ε determines the thickness of the interface. γ = 0.1 and ε = 0.8E-6 are used in our specific simulations.

Second, the electric field in the droplet, oil and dielectric layers is calculated by the Poisson equation:

$$\nabla \cdot (\varepsilon_o \varepsilon_r \nabla \varphi) = \rho_f \qquad (5)$$

where φ is the electric potential, ρ_f denotes the free net charge density, $\varepsilon_0\varepsilon_r$ represents the permittivity of the related medium in the field. The Poisson equation is coupled with the two-phase flow equations through the distribution of different dielectric materials (water, oil, PDMS, and silicon oxide), and the electric field (E) is instantaneously calculated during the droplet splitting and reshaping process. The system capacitance is calculated in the electrostatic interface by:

$$C = \frac{2U_e}{V^2} \qquad (6)$$

$$U_e = \frac{1}{2}\varepsilon_0 \varepsilon_r \int_\Omega |E|^2 d\Omega \qquad (7)$$

where V is the potential difference between the two induction electrodes, U_e and E are the electrical energy stored and the electric field in the domain, respectively. Ω denotes the entire computational domain in the model.

2.3 Device fabrication and instruments

The device consists of a poly(dimethylsiloxane) (PDMS) layer containing microfluidic channels and an electrode-patterned quartz substrate. The microchannels were fabricated in PDMS using a standard soft lithography procedure. A negative photoresist (SU-8 2050, MicroChem) was spin-coated and patterned on a silicon wafer. The developed SU-8 pattern yielded a mold for microchannels of 50 μm deep. PDMS mixture in a 10:1 ratio of prepolymer and curing agent (Sylgard 184, Dow Corning) was degassed and poured over the mold and cured in an 80 °C oven for an hour. The cast PDMS was then peeled off from the mold and inlet and outlet holes were punched using a pan head needle on the PDMS replica. To make the microelectrodes, an adhesive layer of Ti/W (200 Å) and 1500 Å of platinum were sputtered on a photoresist patterned quartz wafer, and a lift-off process was applied to form the electrode patterns. Then an insulation layer of silicon oxide with a thickness of 1 μm was deposited on the patterned quartz substrate using PECVD, and finally the contacting pads for electrical connection were exposed. The PDMS replica and quartz substrate were cleaned, treated with oxygen plasma, aligned under the microscope and then bonded together to seal the microchannels.

Syringe pumps (KD Scientific) were used to deliver the mineral oil and DI water into the microchannels at a range of flow rates. An inverted microscope (Eclipse Ti, Nikon) with a CCD camera (EXi Blue, Q-IMAGING) was used to capture the droplets moving in the microchannels. Two source meters (Keithley 2400) were used to supply DC voltages to the induction and controlling electrodes and monitor the currents spontaneously.

3 Results and discussion

3.1 Splitting and charging process

The dynamic process of droplet splitting and charging was simulated for two designs: a T-shaped microchannel (Fig. 2a) and a modified design with a triangle notch at the T-junction (Fig.2b). The droplet was initially set in rectangular shape (6000 μm^2, estimated from the captured CCD images in experiments) with two parallel aqueous phases in the continuous oil phase. Two electrodes with a length of 100 μm were set symmetrically across the T-junction as indicated. The SiO_2 dielectric layer was modeled as a 1 μm thick line between the electrodes and microchannel walls. The inlet velocity of the continuous phases was set as 28.7 mm/s, in order to match the droplet velocity in the experiments. The physical parameters used in the simulation are summarized in Table 1.

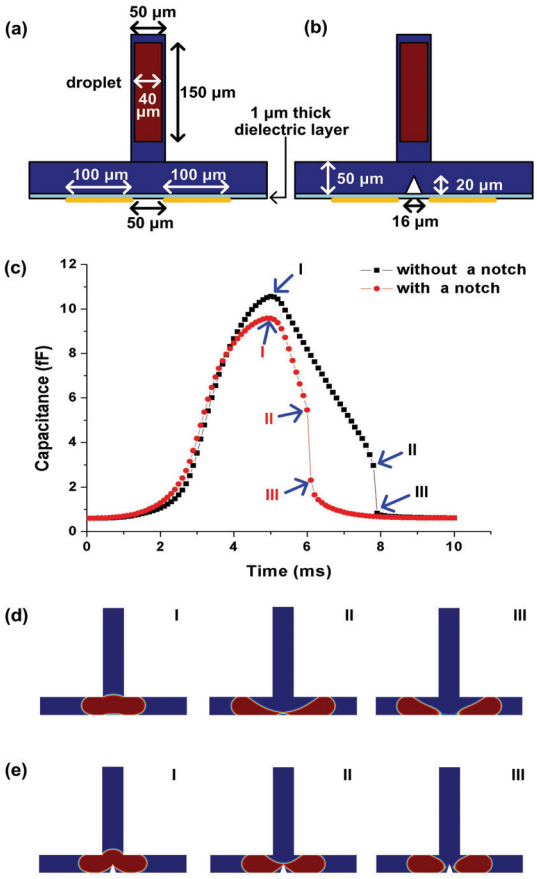

Fig. 2 Simulation of the charging process. (a) and (b) 2D computational domain for the T-channels without and with a notch, respectively. (c) The capacitance of the whole system during the splitting process. (d) and (e) Snap images of the droplets at the critical instants (indicated in Fig. 2c) during the splitting process in the T- channels without and with a notch, respectively.

Table 1 Physical properties

Density of water, ρ_1	1008	kg/m^3
Density of mineral oil, ρ_2	840	kg/m^3
Dynamic viscosity of water, μ_1	1.02	mPa•s
Dynamic viscosity of mineral oil, μ_2	30	mPa•s
Interfacial tension, σ	38	mN/m
Relative dielectric constant of water	78	
Relative dielectric constant of PDMS	2.8	
Relative dielectric constant of mineral oil	2.5	
Relative dielectric constant of silicon oxide	3.9	

The simulation results of the two designs are shown in Fig. 2c-e. The system capacitance is calculated from Eqs. (6) and (7), and its value varies as one droplet travels from the center channel to the T-junction, stretches and splits into two droplets. As shown in Fig. 2c, three critical points (I, II, III) in the time-dependent capacitance curves indicate the corresponding steps (I, II, III) that are depicted in Fig. 2d and e for the two designs, respectively. The system capacitance increases firstly as the droplet moves into the T-junction, and reaches the maximum at point I. This is reasonable, since the permittivity of droplet (water) is much higher than that of the surrounding mineral oil. When the droplet moves closer to the T-junction, more space between two electrodes is filled by water instead of oil. When the space is filled with water (Fig. 2d-I and 2e-I), the system capacitance reaches the maximum. After this moment, the droplet stretches and part of spaces is replaced by oil, which causes the capacitance to drop again. The stretching process and capacitance falling-down trend continue until the R-P instability (when the tinning thread of the droplet starts to break) takes place. Fig.2d-II and 2e-II indicate the instant just before the separation. Then, the liquid thread breaks rapidly (Fig. 2d-III and 2e-III), leading to a sudden drop of the capacitance (as shown in Fig. 2c from point II to point III). Our simulation results are consistent with the work of capacitive sensing of droplets by Elbuken et al.[10], in which they demonstrated that the capacitance firstly increased and then decreased when the droplet entered and left the sensing electrodes, and saturated once the entire droplet was in the sensing region.

As mentioned above, the ultimate net charge in daughter droplets are determined by the capacitance at the instant of separation. However, in the original T-junction, a long and slim liquid thread (Fig.2d-II) would reduce the total capacitance severely (from 10.71 fF to 2.98 fF in our simulation). In order to alleviate this reduction, an isosceles triangle (with a height of 20 μm and a base of 16 μm) shaped notch is symmetrically set at the T-junction to accelerate the R-P instability and speed up the splitting process. The red curve in Fig.2c is the time-dependent capacitance curve for this new design. At the instant of separation, the system capacitance is increased from 2.98 fF to 5.47 fF compared to the original design. As shown in Fig. 2d-II and 2e-II, the break-up of the liquid thread is facilitated by the triangle notch without much stretching and elongation.

3.2 Simulations of droplets of different size

Numerical simulations were performed to study the droplet size effect on the whole system capacitance. The same simulation model was adopted, while the droplet size was changed. The results were shown below in Fig. 3.

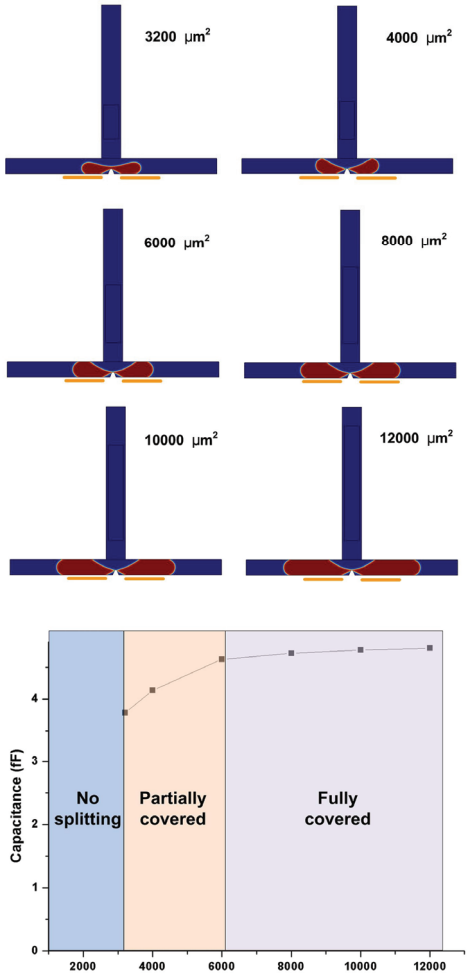

Fig. 3 Simulation results showing the droplet size effect on the system capacitance at the instant of separation. For 'No splitting' region, data of the system capacitance at the separation instant is not available since no separation occurs.

There are three regions as the droplet size increases (3200~12000 μm^2). (1) When the projected area of the droplet is smaller than 3200 μm^2, the droplet can not split at the T-junction.

Negative and positive charges can not be ultimately separated into two daughter droplets and no charges will be obtained in droplets. (2) When droplet area is 3200~6000 μm^2, the droplet can split and partially covers the charging electrodes at the T-junction. In this region, more space across the charging electrodes is covered by water as the droplet size increases, and therefore the whole system capacitance is continuously increasing. (3) When the droplet area is greater than 6000 μm^2, the droplet fully covers the charging electrodes. Then the whole system capacitance gradually approaches a constant value. In summary, the size of the droplet can affect the whole system capacitance and then the ultimate charges in the daughter droplets. For a droplet of specific size, the system capacitance and corresponding induced charge can be obtained from the simulation model.

3.3 Simulations of using surfactant

Use of surfactant could low the interface tension and help stabilize the droplets in microfluidics. Numerical simulations were performed to study the surfactant effect on the whole system capacitance. The same simulation model was adopted. A T-junction without a notch (as shown in Fig. 2a) was used for observing the long and slim liquid thread. The interfacial tension was set from 0.005 N/m to 0.038 N/m (for our mineral oil/water system). The simulation results are shown below in Fig. 4.

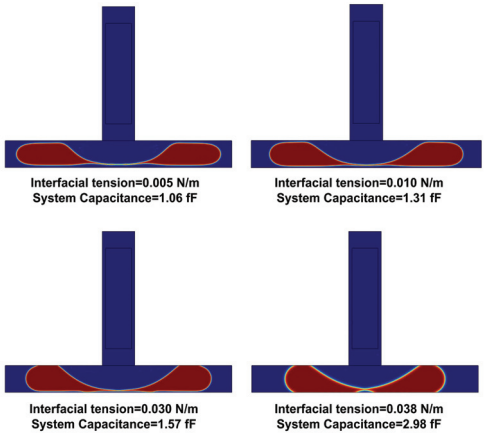

Fig. 4 Simulation results showing the surfactant effect on the droplet elongation and splitting at the separation instant.

3.4 Experimental results

We also experimentally measured the amount of induced charges in droplets for the two designs. In the characterization device, droplets are firstly formed using a flow focusing structure, travel to the T-junction where the droplets are charged and split. Then, these precharged droplets flow into the testing channels for charge quantifitation. As shown in Fig. 5, two testing channels (with a width of 200 μm) and two pairs of deflecting electrodes (with an interval of 240 μm) were added symmetrically on both sides of the T-channel to ensure balanced flow in the device. Droplet displacement was measured in the testing channel in presence of a transverse electric field (E_d).

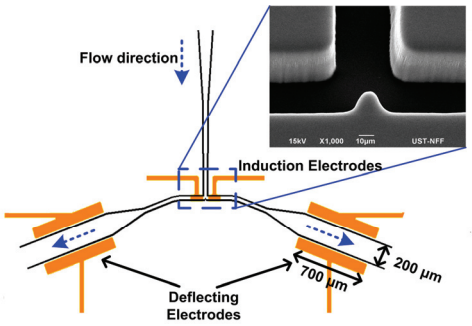

Fig. 5 Schematic illustration of the device for measuring the induced charge in a droplet. The inset is an SEM image of the T-junction with a notch at the center.

The charge quantification is based on a hydrodynamic model of droplet trajectory. In our devices, the droplet charge can be approximated as[11, 12]

$$q = \frac{6\pi \cdot r\eta}{E_d} \cdot \frac{y}{t} \qquad (8)$$

Thus, for a given deflecting voltage, the droplet charge can be obtained by measuring the droplet displacement as a function of the travelling time. In our experiments, a constant voltage of 20 V was applied to the defecting electrodes, and the transverse electric field is estimated to be 83 kV/m. The droplet charge was tuned by the charging voltage (stepping from -50V to 50 V). The displacement of charged droplets in the testing channel was recorded by a CCD camera (as shown in Fig. 6).

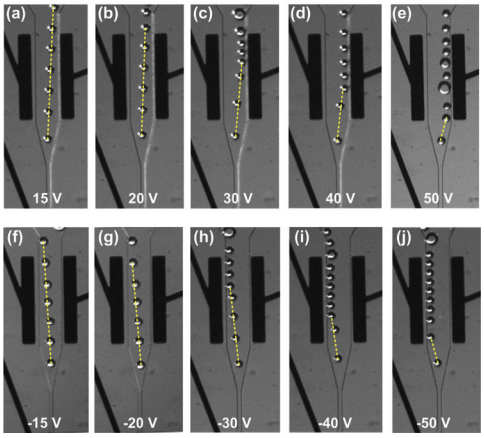

Fig. 6 Deflection of droplets with different amount of charge under a constant deflecting voltage of 20 V. The charging voltage was 15 V for (a), 20 V for (b), 30 V for (c), 40 V for (d), 50 V for (e), -15 V for (f), -20 V for (g), -30 V for (h), -40 V for (i) and -50 V for (j).

In Fig. 6 a-e, the droplets show increasing displacement in the transverse direction as the charging voltage increase from 15 to 50 V. For negative charging voltages, the direction of droplet displacement became opposite and the magnitude changed accordingly. The displacement (y) and the traveling time (t) were directly measured from the CCD images. Then, the amount of induced charge was calculated from Eq. (8) and the value versus the charging voltage (symbols) is plotted in Fig. 7. Solid lines are the simulation results for the fabricated devices of the two designs.

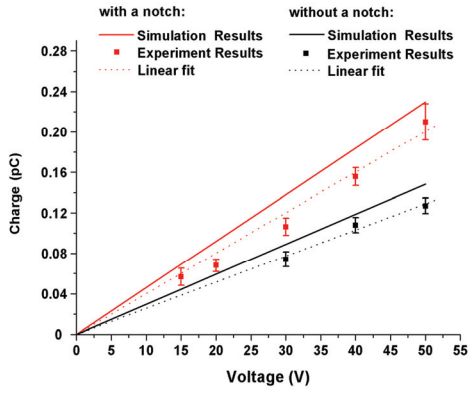

Fig. 7 Induction charge versus charging voltage. The data in the third quadrant (negative charge and voltage) were omitted since they were almost symmetric to the data in the first quadrant.

The slope of the charge-voltage curve represents the system capacitance. The linear fits of the experimental data (dotted lines) yield 4.12 fF and 2.60 fF for the designs with and without a notch, respectively, while 4.61 fF and 2.98 fF were obtained in the simulations. It should be noted that the fabricated notch (inset of Fig. 5) has a round tip instead of a sharp one, reducing the capacitance from 5.47 fF (Fig. 2) to 4.61 fF. The relative errors between experimental and simulation results are within 15%. The discrepancy is mainly due to the two-dimensional (2D) model we adopted in the numerical simulations. Although the 2D model can greatly reduce the computation cost, for this practical 3D problem, it may lead to a certain errors. For example, in the 2D model, the thinning liquid thread is treated as a slice normal to the xy-plane, whereas it should be an asymmetrical cylindrical thread in the 3D model. Therefore, the capacitance in the 3D situation should be lower than the 2D simulation results. Nevertheless, our simulation model has revealed the overall trend of the charging process, and therefore may serve as an effective tool for analyzing and optimizing the designs for droplet-based microfluidics.

Conclusion

In summary, we have numericailly explored the working principle of the non-contact charging system. The simulation was conducted using COMSOL Multiphysics, based on the laminar two-phase flow level-set interface coupling with the electrostatic interface. Meanwile, we have developed a microfluidic device for non-contact electrostatic charging of droplets. Both simulation and experimental methods matched well with each other. We expect our work could enable precision manipulation of droplets for more complex liquid handling in microfluidics and promote electric-force based manipulation in 'lab-on-a-chip' systems.

Acknowledgements

This work was supported by the Direct Allocation Grant (No. DAG12EG07-13) from HKUST and the National Science Foundation of China (No. 61006086).

Reference

1. Franke, T.A. and A. Wixforth, *Microfluidics for miniaturized laboratories on a chip, ChemPhysChem*. **9**, 2140-2156 (2008).
2. Zhou, H., G. Li, and S. Yao, *A droplet-based pH regulator in microfluidics, Lab on a Chip*. **14**, 1917-1922 (2014).
3. Atencia, J. and D.J. Beebe, *Controlled microfluidic interfaces, Nature*. **437**, 648-655 (2004).
4. Stone, H.A., A.D. Stroock, and A. Ajdari, *Engineering flows in small devices, Annu. Rev. Fluid Mech.* **36**, 381-411 (2004).
5. Zhou, H. and S. Yao, *Electrostatic charging and control of droplets in microfluidic devices, Lab on a Chip*. **13**, 962-969 (2013).
6. Link, D., S.L. Anna, D.A. Weitz, et al., *Geometrically mediated breakup of drops in microfluidic devices, Physical review letters*. **92**, 54503 (2004).
7. Carlson, A., M. Do-Quang, and G. Amberg, *Droplet dynamics in a bifurcating channel, International Journal of Multiphase Flow*. **36**, 397-405 (2010).
8. Jiang, L., Y. Zeng, H. Zhou, et al., *Visualizing millisecond chaotic mixing dynamics in microdroplets: A direct comparison of experiment and simulation, Biomicrofluidics*. **6**, 012810 (2012).
9. Sussman, M., P. Smereka, and S. Osher, *A Level Set Approach for Computing Solutions to Incompressible Two-Phase Flow, Journal of Computational Physics*. **114**, 146-159 (1994).
10. Elbuken, C., T. Glawdel, D. Chan, et al., *Detection of microdroplet size and speed using capacitive sensors, Sensors and Actuators A: Physical*. **171**, 55-62 (2011).
11. Ahn, B., K. Lee, R. Panchapakesan, et al., *On-demand electrostatic droplet charging and sorting, Biomicrofluidics*. **5**, 024113 (2011).
12. Guo, F., X.H. Ji, K. Liu, et al., *Droplet electric separator microfluidic device for cell sorting, Applied Physics Letters*. **96**, 193701 (2010).